Band-Gap Landscape Engineering in Large-Scale 2D Semiconductor van der Waals Heterostructures

Victor Zatko, Simon Mutien-Marie Dubois, Florian Godel, Cécile Carrétéro, Anke Sander, Sophie Collin, Marta Galbiati, Julian Peiro, Federico Panciera, Gilles Patriarche, et al.

ACSNANO

www.acsnano.org

ARTICLE

Band-Gap Landscape Engineering in Large-Scale 2D Semiconductor van der Waals Heterostructures

Victor Zatko, Simon Mutien-Marie Dubois,[#] Florian Godel, Cécile Carrétéro, Anke Sander, Sophie Collin, Marta Galbiati, Julian Peiro, Federico Panciera, Gilles Patriarche, Pierre Brus, Bernard Servet, Jean-Christophe Charlier, Marie-Blandine Martin, Bruno Dlubak,* and Pierre Seneor*

Cite This: https://doi.org/10.1021/acsnano.1c00544

Read Online

ACCESS | Metrics & More | Article Recommendations

ABSTRACT: We present a growth process relying on pulsed laser deposition for the elaboration of complex van der Waals heterostructures on large scales, at a 400 °C CMOS-compatible temperature. Illustratively, we define a multilayer quantum well geometry through successive *in situ* growths, leading to WSe_2 being encapsulated into WS_2 layers. The structural constitution of the quantum well geometry is confirmed by Raman spectroscopy combined with transmission electron microscopy. The large-scale high homogeneity of the resulting 2D van der Waals heterostructure is also validated by macro- and microscale Raman mappings. We illustrate the benefit of this integrative *in situ* approach by showing the structural preservation of even the most fragile 2D layers once encapsulated in a van der Waals heterostructure. Finally, we fabricate a vertical tunneling device based on these large-scale layers and discuss the clear signature of electronic transport controlled by the quantum well configuration with *ab initio* calculations in support. The flexibility of this direct growth approach, with multilayer stacks being built in a single run, allows for the definition of complex 2D heterostructures barely accessible with usual exfoliation or transfer techniques of 2D materials. Reminiscent of the III−V semiconductors' successful exploitation, our approach unlocks virtually infinite combinations of large 2D material families in any complex van der Waals heterostructure design.

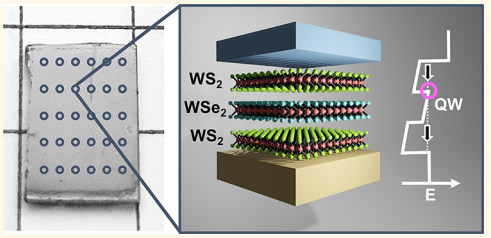

KEYWORDS: *2D semiconductors, van der Waals heterostructure, pulsed laser deposition, quantum well, tungsten disulfide, tungsten diselenide*

INTRODUCTION

Two-dimensional semiconductors have been hailed as ultimately thin functional electronic materials, with potential applications for instance in electronics, optoelectronics, and spintronics.[1−5] Their assembly into heterostructures with atomic precision is expected to lead to a wealth of properties and device structures,[6−8] reminiscent of the successful exploitation of III−V semiconductor families.[9−15] Indeed, the precise band-gap landscape engineering allowed by 2D material stacking promises eased functional structure definition, including atomically defined quantum wells and vertical superlattices such as quantum cascades. This vision is fueled by the extremely large extension of 2D material families being now uncovered with fine modulation of their properties by their atomic composition (including doping and alloying),[8,16−18] adjacent crystallography angle control,[19,20] and proximity effects maximized by their atomic 2D geometry.[21−23] Illustratively, beyond elemental 2D materials such as silicene and phosphorene, large varieties of mono-, bi-, and trichalcogenides are identified and studied. These anticipated functional 2D heterostructures are expected to also include exotic phenomena, illustrated by unconventional "magic-angle" superconductivity and ferroelectricity, as well as other in-plane moiré-superlattice-related properties already observed in graphene/graphene or graphene/h-BN stacks.[24−29]

This extreme versatility of band-gap landscapes in 2D semiconductor heterostructures is a strong asset for applications such as radio frequency (and above) and optoelectronic devices, generating for instance high expect-

Received: January 20, 2021
Accepted: March 16, 2021

ations for van der Waals heterostructure field-effect transistors or excitonic control.[30−32] Concerning spintronics, the quest for material platforms seeking unconventional functionalities and increased performances is sustained by MRAM spin circuit developments[33−35] and post-CMOS spin-based visions[36,37] (including stochastic,[38] neuromorphic,[39] and quantum calculations[40]). In this direction, the atomic thickness definition of van der Waals heterostructures and specific properties of 2D materials are seen as a strong potential for spin control.[4,41] Already, the use of 2D materials in spintronic devices led to the observation of efficient spin-filtering properties,[23,42] as well as strong potential for tailoring the perpendicular magnetic anisotropy,[43−45] spin−orbit torques (SOT),[46] and skyrmionics topological spin textures.[47,48] Two-dimensional material heterostructures thus appear as a promising target for the fabrication of ultrathin, highly tailorable and gatable devices toward spin transport and manipulation.

While van der Waals heterostructures thus generate particularly high expectations, their exploration calls for a systematic route for their assembly. Indeed, the mechanical exfoliation approach,[49] augmented by pickup techniques for stacking,[50] already allowed pioneer studies of fundamental properties but came with limitations in size, reproducibility, and interface control. These pioneering but tedious manual approaches also came with realistic limitations in terms of 2D heterostructure unit cell repetition. In the specific case of spintronics, interface preservation of fragile spin sources has also been a constant difficulty for 2D material integration in spin-valve structures.[51] Fortunately, other 2D mode growth techniques have been developed. In particular the successful growth of graphene—the prototypical 2D material—by CVD has demonstrated the feasibility to grow and, importantly, integrate 2D crystals on large scales.[52] However, this direct growth of large graphene layers has relied on long-studied and harnessed catalytic properties of substrates[53,54] and proved to be more difficult to extend to other 2D materials and heterostructures in a direct way. Even with pioneer demonstrations for CVD growth of h-BN and 2D semiconductors such as MoS_2 and WS_2,[55−57] this technique has remained challenging for any given 2D material, and heterostructures are still mainly defined today through layer-by-layer transfer protocols when possible. This limits 2D heterostructure scaling and complicates the integration of the most fragile 2D materials in functional van der Waals heterostructures. Interestingly, in addition to CVD fundamental studies, while less studied, promising alternative growth approaches have been presented relying on molecular beam epitaxy or pulsed laser deposition (PLD) techniques.[58−62] These approaches have been traditionally well adapted and demonstrated to define complex heterostructures for common metals, semiconductors, and oxides.

In this study we present an approach to derive functional van der Waals stacks of 2D semiconductors using PLD. We focus on two reference 2D semiconducting materials, WS_2 and WSe_2, to illustrate the flexibility offered by PLD: simply by switching targets we are able to fabricate *in situ* a $WS_2/WSe_2/WS_2$ heterostructure (Figure 1). We probe by Raman spectroscopy the good crystallization of both WS_2 and WSe_2 and show by structural (transmission electron microscopy) and chemical analyses (energy-dispersive X-ray spectroscopy) that we indeed derived a well-defined heterostructure of 2D materials (Figure 2). Raman spectroscopy mappings on both macroscopic and microscopic scales demonstrate the high homogeneity of the

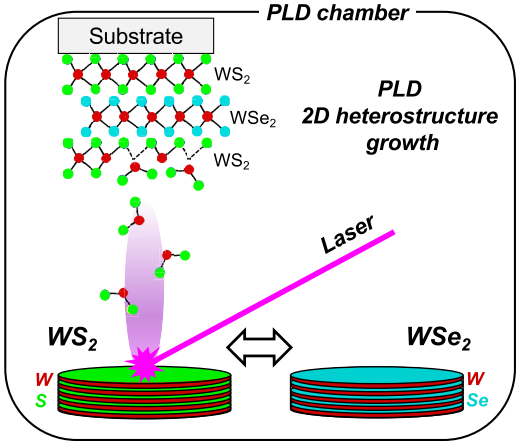

Figure 1. Schematic view of the 2D heterostructure PLD growth process. Stoichiometric targets of selected TMDC 2D semiconductors are ablated using a tripled frequency Nd:YAG laser (355 nm) in a 10^{-1} mbar high-purity Ar atmosphere, introduced in the 1×10^{-8} mbar base pressure customized PLD chamber. The PLD approach offers direct integration of 2D materials in van der Waals heterostructures with eased stacking by simple *in situ* target change.

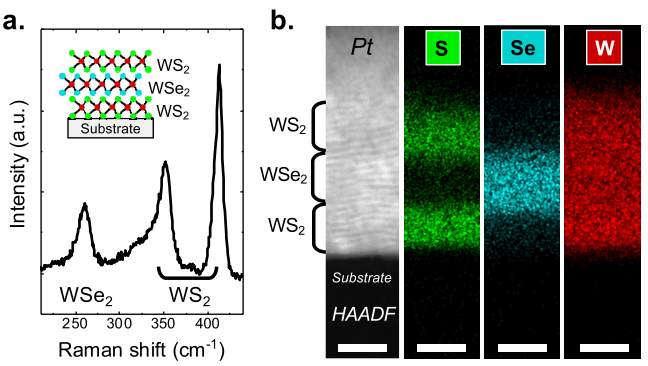

Figure 2. (a) Raman spectrum recorded on the resulting $WS_2/WSe_2/WS_2$/Ni sample with a 514 nm laser and 5 mW power. Clear Raman signatures of both materials are recorded. (b) (Left) TEM image taken in HAADF mode of the 2D $WS_2/WSe_2/WS_2$ heterostructure capped by Pt during TEM membrane preparation. Lamellar layers of the 2D materials are clearly visible traducing their high crystallinity. (Right) Corresponding chemical analyses by EDX mapping of S, Se, and W levels. S and Se chemical areas correspond to the expected $WS_2/WSe_2/WS_2$ stacking. White scale bar is 10 nm for all images.

fabricated heterostructure (Figure 3). Already, we put forward the benefit of the *in situ* PLD approach beyond flexibility and large scale, as this allows us to integrate even delicate 2D materials without exposing them to air. Indeed, 2D materials such as WSe_2 are known to deteriorate on relatively short time scale, but here their direct integration in a van der Waals heterostructure is shown to preserve their properties over extended periods (Figure 4). Finally, we present transport measurements (Figure 5) illustrating the benefit of 2D van der Waals heterostructure engineering for the tailoring of a band-gap energetic landscape, as highlighted by *ab initio* calculations (Figures 6−8). Overall this PLD approach offers a very convenient point of entry for the exploration of complex 2D van der Waals heterostructures for electronics and spintronics.

https://doi.org/10.1021/acsnano.1c00544
ACS Nano XXXX, XXX, XXX−XXX

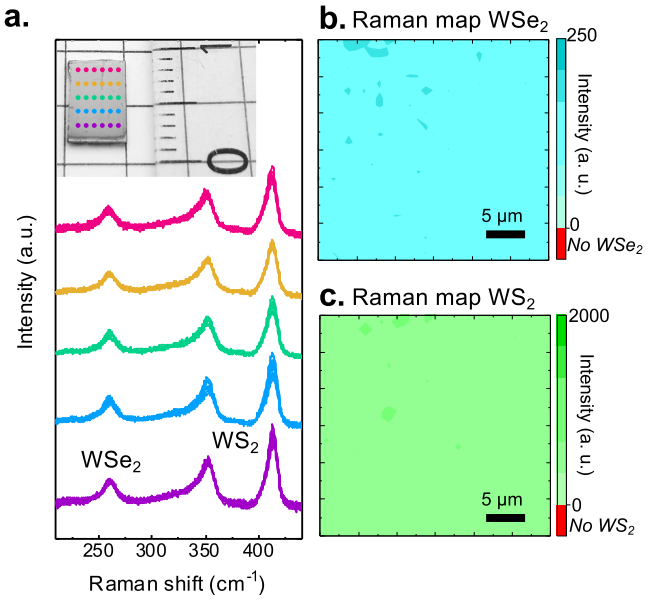

Figure 3. (a) Raman spectra recorded on cm^2 scales on the WS_2/WSe_2/WS_2/Ni sample (optical image in inset) with a 514 nm laser and 5 mW power: each point on the optical image corresponds to a given Raman spectrum, and all Raman spectra of the same line have been plotted on top of each other and represented by one given color. All spectra show similar WS_2 and WSe_2 presence: the heterostructure has been homogeneously grown on the whole substrate surface. (b and c) Raman intensity map of the WSe_2 peak and A_{1g} WS_2 peak, respectively, recorded each 1 μm on the same 30 μm by 30 μm area. High homogeneity on a local scale is noted as well. Overall, both maps (local and cm^2) show the large-scale full coverage of the 2D WS_2/WSe_2/WS_2 heterostructure over the Ni substrate.

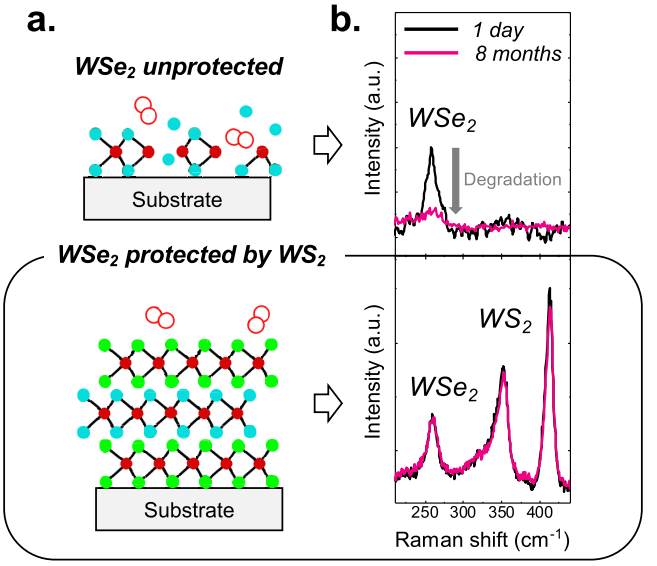

Figure 4. (a) Schematic picture of WSe_2 alone and WS_2/WSe_2/WS_2 heterostructure evolution after air exposure. (b) Raman spectra recorded on WSe_2 (top) and WS_2/WSe_2/WS_2 (bottom) samples with a 514 nm laser after 1 day (black curve) and 8 months (pink curve) of air exposure. Without protection, WSe_2 deteriorates and crystalline order is no longer visible on the Raman spectrum after 8 months in ambient conditions. On the contrary, while encapsulated in WS_2 layers, WSe_2 presents unchanged Raman spectra over the long observation period. WSe_2 is protected from degradation when embedded in the WS_2 sandwich.

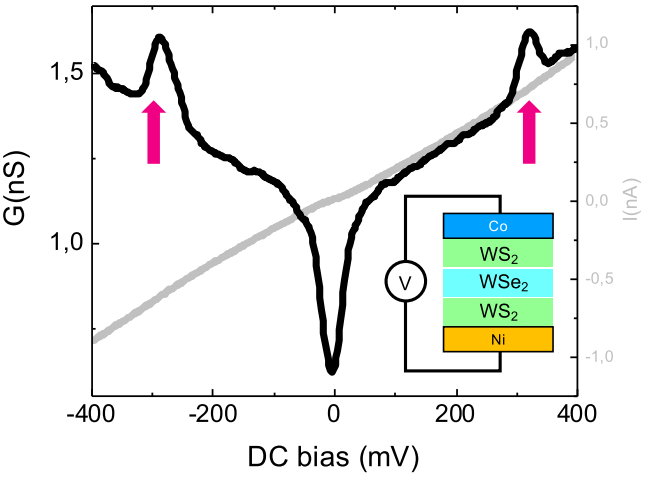

Figure 5. Transport measurements in van der Waals 2D semiconductor heterostructures. I(V) and G(V) measurements obtained in a 1 μm^2 junction of Co/WS_2/WSe_2/WS_2/Ni at 2 K (inset scheme of the junction). Symmetric resonances at ±300 mV are observed, emanating from the engineered quantum well energetic landscape in the 2D semiconductor stack.

RESULTS AND DISCUSSION

In Figure 1 we show the general principle of the heterostructure growth by pulsed laser deposition. We use a customized PLD growth chamber at a base pressure of 1 × 10^{-8} mbar and equipped with a tripled-frequency Nd:YAG laser (355 nm). The key to 2D heterostructure growth following this PLD approach is the ability to switch material targets *in situ*. Here we focus on two reference 2D semiconductor transition metal dichalcogenide (TMDC) lamellar materials: WS_2 and WSe_2. The commercial stoichiometric targets (from Neyco) of WS_2 and WSe_2 are preablated in the Ar atmosphere of the chamber before deposition. The substrate is fixed at a large distance of 70 mm from the target, and the Ar pressure in the chamber is kept at a high value of 10^{-1} mbar to mitigate the plume energy and allow lateral crystallization to take place.[62−64] During growth, each target is shot for 1 min with 80 mJ laser power pulses (2.5 Hz repetition frequency) while the sample is heated at a CMOS-compatible temperature of 400 °C. Crucially, changing the material targets *in situ* allows alternating the 2D layer stack deposition without exposing interfaces to air. We focus here on a simple quantum well definition, formed by buried WSe_2 embedded in-between two WS_2. All these layers are grown with the same PLD parameters. Finally, once the van der Waals heterostructure is grown, the sample is left to cool in Ar for 1 h.

We then analyze the resulting deposited layer to highlight the growth of a semiconducting van der Waals heterostructure, as presented in Figure 2. We first carry out a Raman spectroscopy study to probe the crystalline structure of the deposited layered film. Indeed, Raman spectroscopy gives rise to a clear and distinct signature for both WS_2 and WSe_2 2D semiconductors.[42,62,65−68] We make use of a Renishaw Raman spectrometer with a 514 nm laser. Interestingly, as displayed in Figure 2a, several peaks appear in the Raman response for every probed location, corresponding to both WS_2 and WSe_2 2D crystallographic structures. Concerning WS_2, two Raman signature peaks are expected in the 200− 500 cm^{-1} range:[42,62,65] the Raman spectra show characteristic phonon peaks of 2LA + E_{2g} modes at about 350 cm^{-1} and a first-order

https://doi.org/10.1021/acsnano.1c00544
ACS Nano XXXX, XXX, XXX−XXX

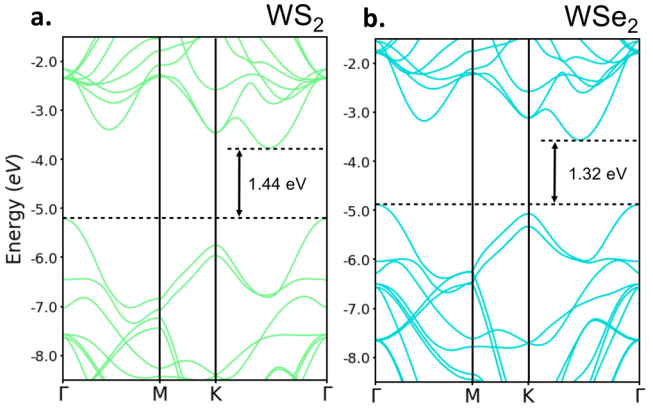

Figure 6. Band structures of bulk WS_2 and WSe_2 computed at the G_0W_0 level. The zero of energy is taken as the vacuum energy level. The valence band maximum and conduction band minimum, corresponding to the ionization potential and electronic affinity, are indicated using dotted horizontal lines. The values of the indirect band gap are also presented to ease the comparison, highlighting a staggered gap in the grown heterostructure.

mode A_{1g}/A1′ at about 420 cm^{-1}. The clear observation of these two Raman peaks in Figure 2a thus confirms the presence of the WS_2 semiconductor in the grown heterostructure. Similarly, for WSe_2, a distinctive Raman signature is expected in this range, with the most prominent Raman peak for bulk WSe_2 expected at ∼250 cm^{-1}.[66−68] While A_{1g} and E_{2g} modes are well separated for many reference TMDCs such as WS_2, they are almost degenerate for WSe_2, resulting in the presence of a single broad peak at lower wavenumbers. This peak is well observed in our case as expected just above 250 cm^{-1} (Figure 2a) and confirms the presence of WSe_2 in our stack. These first spectroscopy analyses already highlight that we have been able to grow the two different TMDC 2D semiconductors during our sequential growth process.

To directly verify the organization of the 2D heterostructure in the *z* axis direction, we further carry out TEM analyses (Figure 2b). Indeed, a high lateral organization (ordered 2D layer-by-layer growth mode) is expected to allow building enough atomic contrast to observe 2D planes. This type of observation on van der Waals heterostructures has previously been carried with stacked exfoliated 2D materials.[69] The exfoliation approach indeed offers high in-plane organization, at the cost of manual stacking efforts with ultraclean stamping protocols and localized flakes at the micron scale. In our case, with the 2D heterostructure sample being close to the cm^2 scale, only a regular lateral section preparation is required. After adapted carbon and Pt protective capping, a focused ion beam (FIB) is used to micromachine a thin electron-transparent lamella for cross-sectional TEM analysis through a lateral section of the sample. TEM images were acquired *ex situ* with a Themis (Thermo Scientific) STEM equipped with a Super-X EDX detector and operated at 200 kV. A typical representative image of a section of the heterostructure is presented in Figure 2b. We observe the lamellar organization of the heterostructure, with about 3 × 8 2D layers, showing long-range crystallization and a *z*-axis stacking as expected from measured Raman signatures. This observation further confirms the fabrication of the targeted 2D semiconducting van der Waals heterostructure. To further highlight the well-defined organization of the grown 2D materials in a quantum well geometry, we carry out chemical EDX spectroscopy in the same observed position as the TEM image (Figure 2b). The EDX analysis reveals the expected organized alternation of W−Se and W−S materials, matching with the measured Raman signal of both WS_2 and WSe_2 2D layers. The heterostructure is thus showing lamellar organization with stacking of the different 2D semiconductors defined by the PLD growth order. Overall, we illustrate here that our PLD approach indeed resulted in the targeted 2D semiconductors organized in a well-defined $WS_2/WSe_2/WS_2$ van der Waals heterostructure. This result is particularly striking, as it shows that complex compositions and multiple stacking of 2D materials on large scales are at hand, thanks to the high flexibility offered by PLD.

A strong asset of the PLD approach is its ability to fabricate large-scale materials compared to pioneer exfoliation and pick-up-transfer experiments. To highlight this aspect, we thus explore the homogeneity of the deposited van der Waals heterostructure over the whole sample surface. In this direction we carry out both macro- (Figure 3a) and micro- (Figure 3b and c) scale Raman spectroscopy mappings. In Figure 3a we probe the crystallographic order in a matrix set of positions covering the whole surface of the sample. We systematically record Raman spectra at each position, with experimental parameters corresponding to Figure 2a. As displayed in Figure 3a, the $WS_2/WSe_2/WS_2$ Raman signatures as detailed above appear in every position of the sample: the three signature peaks of our heterostructure (WSe_2 $A1_g + E_{2g}$ mode, WS_2 2LA + E_{2g} mode, WS_2 A_{1g}/A1′ mode) are observed for all measurements. We observe no notable variations on these large scales, with similar amplitude, shape, and position for each peak. This Raman survey shows that we defined the van der Waals heterostructure on the whole sample surface. This is to be contrasted with other approaches, in particular

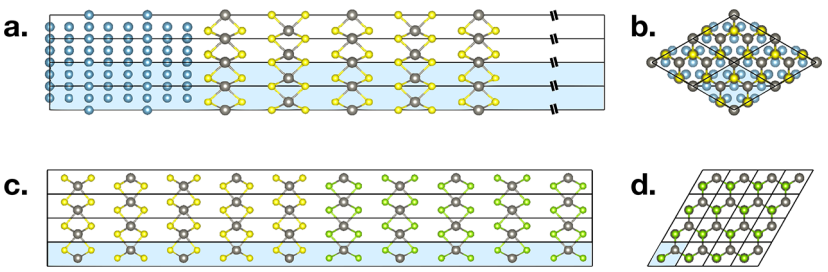

Figure 7. Ball-and-stick representation of two of the lattice-matched interfaces computed to estimate the natural band offsets in the functional van der Waals device. (a, b) Side and top views of the computed Ni/WS_2 lattice-matched supercell. A vacuum slab of 20 Å is included in the cell. (c, d) Side and top view of the WS_2/WSe_2 lattice-matched interface. The computational unit cell is colored in blue. Ni, W, S, and Se atoms are respectively represented as blue, gray, yellow, and green spheres.

https://doi.org/10.1021/acsnano.1c00544
ACS Nano XXXX, XXX, XXX−XXX

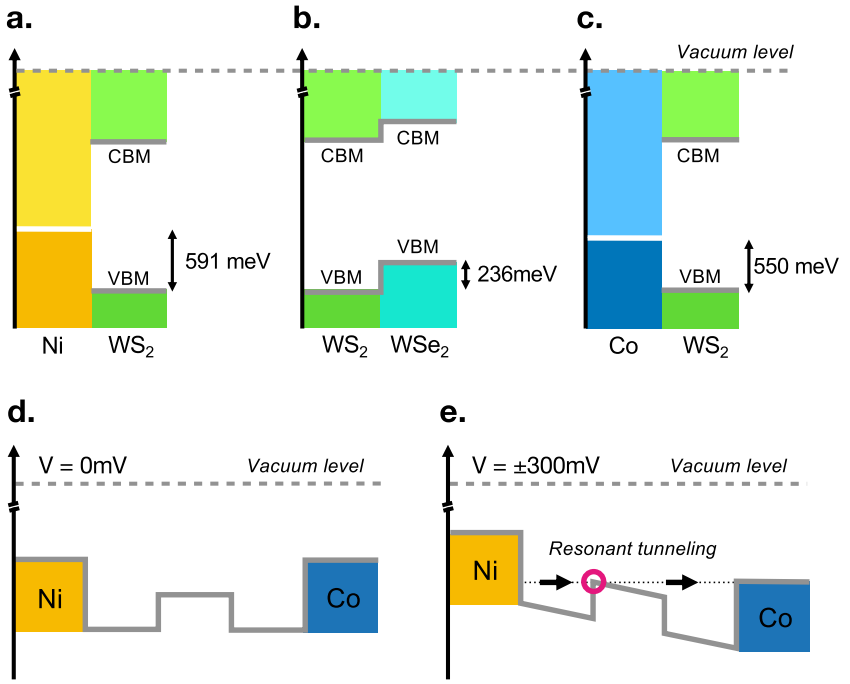

Figure 8. Schematization of the energy profiles across the device. (a–c) Computed band offsets at the various interfaces of the contacted van der Waals heterostructure: (a) Ni/WS_2, (b) WS_2/WSe_2, (c) Co/WS_2. The Fermi levels of Ni and Co are depicted as white lines; the valence band maximum (VBM) and conduction band minimum (CBM) of WS_2 and WSe_2 are depicted as gray lines. The vertical bars indicate the computed band offsets. (d, e) VBM energy profile across the device (d) at equilibrium and (e) at resonance. The resonance corresponds to the specific conductance peaks measured experimentally at 300 mV bias. Overall this confirms the quality of the grown van der Waals heterostructure by our PLD approach and the modularity of their transport properties.

exfoliation, which leads to samples limited in size even for single crystals (isolated WS_2 layers of few tens of μm^2). Furthermore, in Figure 3b and c we check the continuity of the layers by carrying out very dense mappings of Raman measurements. The Raman modes' peak intensities are extracted, allowing us to highlight the presence of the heterostructure: in particular we note no discontinuity in these mappings and excellent homogeneity. Overall, these measurements show complete coverage with both WS_2 and WSe_2 layers with high homogeneity over the $>10^7 \mu m^2$ sample area.

Beyond versatility and large-scale homogeneity, we now further illustrate the benefit of the direct *in situ* definition of 2D heterostructures by the PLD approach. A difficulty appearing with many families of 2D materials concerns their limited stability in ambient conditions. This in turn limits both their exploration by exfoliation and also their growth on a larger scale and transfer, as is usually done with CVD-grown materials using resist-assisted wet etching of catalytic substrates. The versatility of PLD and the *in situ* growth of the heterostructure allows, on the contrary, burying the fragile 2D material layers below another stable 2D material. Two dimensional materials are known to be particularly efficient at quenching the diffusion of species;[70,71] this leads to a very direct and natural way to define a heterostructure encompassing even the most fragile 2D materials. Here we focus on WSe_2, known to progressively degrade when exposed to ambient conditions, with O species replacing Se atoms in the crystal. In Figure 4a we illustrate this with the study of an isolated WSe_2 layer grown by PLD in the exact same conditions as the WSe_2 of the heterostructure. It is observed that after several months of ambient atmosphere exposure the layer is strongly deteriorated, as demonstrated by the evolution of its Raman signature. The main signature Raman peak at about 250 cm^{-1}, corresponding to the WSe_2 $A1_g + E_{2g}$ modes, has vanished. As a comparison, in Figure 4b we show the same time-dependent study of the van der Waals heterostructure with a buried WSe_2 layer. The sample is similarly stored in ambient atmosphere as in Figure 4a. In contrast, after 8 months of study, no change is observed for the signature of the WSe_2 layer, demonstrating that the *in situ* growth of the heterostructure allowed preserving the WSe_2 layer against the adverse reactivity with the ambient atmosphere. This observed preservation of the crystal structure represents a strong asset of the PLD approach. By simply changing material targets *in situ*, it allows the definition of complex heterostructures without any detrimental exposition and manipulation in an open atmosphere. The properties of the selected materials are thus stabilized in the van der Waals 2D heterostructure.

Finally, we illustrate the potential of PLD growth of van der Waals heterostructures for direct integration in functional devices. We show a device fabrication based on the above studied WS_2/WSe_2/WS_2 2D heterostructure with a tailored well-type energetic landscape. We use the Ni(111) substrate as a conductive bottom electrode for our devices.[72] We then carry out a laser lithography step on a spin-coated UVIII resist layer to open small 1 μm^2 windows above the van der Waals heterostructure. A top Au-capped Co electrode is finally deposited by e-beam evaporation. This defines 1 μm^2 microjunctions. We bond them in a ceramic chip and measure the resulting devices at 4 K in an AC + DC cryogenic setup. We show in Figure 5 the resulting dI/dV characteristic measured in such a device. The high resistivity confirms that the current is flowing in the contacted layered structure, as

https://doi.org/10.1021/acsnano.1c00544
ACS Nano XXXX, XXX, XXX–XXX

expected from the material characterization described above. Furthermore, we measure very specific conductance peaks in these structures at about 300 mV. The observation of these peaks demonstrates that a specific resonant energy is defined in our heterostructure. This confirms that the well-type energy band-gap landscape that we engineered by the stacking of the different 2D semiconductors has indeed been achieved, allowing tailoring of charge transport properties.

We further discuss the expected band structure of the stacked 2D layers and how this corresponds to our vertical transport measurements and the observed resonance. We analyze the experimental measurements by performing computational analyses of the 2D van der Waals heterostructure. The band structures of WS_2 and WSe_2 have been previously separately calculated, as well as many available 2D semiconductors of the TMDC family.[42,73] Here we aim more specifically at describing how the energy levels of each material align once gathered in a heterostructure and how this defines the energetic profile of the final device. In this direction we use first-principles calculations to estimate the natural band offsets in the $WS_2/WSe_2/WS_2$ device (see Methods). At first, we use the Kohn−Sham (KS) density functional theory (DFT)[74,75] and the GW approximation to many-body perturbation theory[76,77] to compute the ionization potential (IP), electron affinity (EA), and band structures of bulk WS_2 and WSe_2 using the experimental lattice constants and internal coordinates.[78] Here the IP is evaluated by electrostatic alignment of bulk and surface calculations. The EA is obtained by subtracting the computed GW band gap from the IP. The computed band gaps, IPs, and EAs are reported in Table 1. These are in good agreement with previous estimations and with experimental values.[79−83] The IP is used to align the band structure of both materials against the vacuum level, providing a first estimation of the band discontinuity at the interface. Figure 6a and b reveal a staggered gap (type II heterojunction) at the WS_2/WSe_2 interface.

Table 1. Extracted Parameters for Bulk WS_2 and WSe_2 2D Semiconductors in the Heterostructure (See Methods): Ionization Potential (IP), Electronic Affinity (EA), and Band Gaps, Direct and Indirect[a]

2D semiconductor	IP	EA	ΔE_{gap}^{direct}	$\Delta E_{gap}^{indirect}$
WS_2	5.21	3.77	2.30	1.44
WSe_2	4.89	3.57	1.95	1.32

[a]All values are expressed in eV.

The direct consideration of a lattice-matched interface between WS_2 and WSe_2 (see Figure 7) allows proceeding further with the calculation of the natural band offsets. Here we follow the procedure described by Hinuma *et al.* to compute the band offsets while accounting for the relaxation of the in-plane lattice parameters.[84] The same approach is used to estimate the natural position of Ni and Co Fermi levels with respect to the WS_2 valence band maximum. The computed band offsets at the three considered interfaces are depicted in Figure 8a−c. The natural band offset calculation confirms the staggered gap anticipated at the WS_2/WSe_2 interface (Figure 8b). The profile of the valence band maximum (VBM) across the junction exhibits a 236 meV discontinuity at the WS_2/WSe_2 interface, leading to the realization of a quantum well in the functional device. The Fermi levels of the Ni and Co metallic electrodes are reported respectively at 591 and 550 meV above the VBM of WS_2. While the exact positions of these levels closely depend on the electrostatic nature of the metal−semiconductor interfaces, the relatively similar values obtained by calculations for both the Ni/WS_2 and Co/WS_2 interfaces are consistent with the symmetric transport behavior observed in our functional device. Overall, the computed VBM profile across the junction supports the interpretation of the measured conductance peaks in terms of resonant hole transport through a quantum well at the Γ points defined by our van der Waals heterostructure. The resonance mechanism leading to the transport signature observed is illustrated in Figure 8d and e. The applied bias on the device structure shifts the energy levels of the quantum well until a resonant tunneling situation is reached at an applied bias of about 300 mV. Here, the slight difference in voltage of the peak's positions can be ascribed to the Ni and Co work functions' position relative to the WSe_2 VBM. Beyond attesting the pertinence of the presented PLD approach to fabricate well-defined large-scale van der Waals heterostructures, the strong agreement between the calculations' prediction for the heterostructure behavior and the measured transport properties in the devices further draws a path toward the precise tailoring of band structure properties in these systems.

The global Raman and transport studies highlighted a viable growth path that led to the fabrication of functional quantum well junctions based on these large-area 2D material heterostructures. This demonstrator PLD *in situ* process flow provides cm^2 dimensions for direct 2D material heterostructure stacking, with high versatility. It provides an essential technological step toward reaching early access to 2D van der Waals technologies and components, easing the identification of relevant 2D-based structures before further scaling. We deliver an approach that can be generalized with a wealth of 2D material growths and heterostructure configurations remaining to be explored. We believe that by demonstrating complex stacking of heterostructures with large-scale homogeneity, stack encapsulation, and stability for devices, this study could become a pivotal reference to illustrate how to design and handle functional complex van der Waals heterostructures, all the more as they are increasingly considered for a wide range of applications, including electronics and spintronics. We foresee, for instance, that epitaxial and rotated stackings[85−87] could be further crafted through both growth kinetics control and careful selection of successively grown 2D materials with subtly varied crystallographic properties (lattice parameters). Our tailorable *in situ* PLD approach for 2D heterostructure definition unlocks in particular this latter opportunity. We anticipate thus many parameters to be further studied and exploited for charge/spin transport in targeted functional heterostructures: growth kinetics, stacking order, induced rotations and strains, doping, thickness, 2D materials composition including alloying, *etc.*

CONCLUSION

Overall, we show in this study that van der Waals heterostructures can be conveniently built on large scales through the PLD approach. To illustrate this, we demonstrate the fabrication at low, 400 °C CMOS-compatible temperature of a reference $WS_2/WSe_2/WS_2$ stack, showing both homogeneous material growth on large samples and well-defined heterostructure-related transport characteristics. The extracted transport features from devices are driven by the association of specific band structures of the selected 2D semiconductors in a

https://doi.org/10.1021/acsnano.1c00544
ACS Nano XXXX, XXX, XXX−XXX

quantum-well-type energetic landscape, as illustrated by the presented *ab initio* calculations. We envision that through the same concept easy *in situ* and large-scale heterostacking of multiple 2D materials could be achievable, with hundreds of 2D materials and their 2D alloys virtually accessible by the PLD approach. This large playground for heterostructure engineering with 2D materials unlocked by the PLD approach is reminiscent of the successful applicative exploitation of III−V semiconductor families.[9−15] Our work is thus a step toward the fabrication of advanced transport functions modulated by the insertion and combination of the large families of 2D materials now being uncovered and characterized.

METHODS

Two-Dimensional Semiconductor Heterostructure Growth. A customized PLD setup with a base pressure of 1×10^{-8} mbar is used, with an *in situ* target change system. Before growth, the substrate surface is prepared by preheating at 400 °C in the deposition chamber with 0.1 mbar Ar pressure. Two-dimensional semiconductor heterostructures are derived by the use of commercial stoichiometric targets of WS_2 and WSe_2 bought from Neyco (1(W):2(S,Se) targets with purity >99.9%). The targets are shot with a Nd:YAG laser (wavelength reduced to 355 nm, 80 mJ laser power, 7 ns pulse length, laser pulse frequency of 2.5 Hz) at 0.1 mbar of Ar. The 2D semiconductors target surfaces are first recovered by preablation, without exposing the sample, during 5 min at 0.1 mbar Ar pressure. Each 2D semiconductor layer is then sequentially grown by ablation of a selected target during 1 min, while the sample temperature is kept at 400 °C. Crucially, high-quality growth is observed with a distance between target and substrate fixed at 70 mm. Finally, the sample is cooled in the PLD chamber during 1 h under 0.1 mbar of Ar pressure before further manipulations.

Van der Waals Heterostructure Device Fabrication. A modified Plassys sputtering setup is used to grow the bottom Ni(111) electrode on sapphire. Using the PLD process, the large-scale 2D semiconductor heterostructure is then directly grown on top of this electrode. Device geometries are lithographed by a KLOE laser lithography system, leading to 1 μm^2 junctions in UVIII resist. E-beam evaporation is used to deposit top gold capped Co contacts on the van der Waals heterostructure through the microjunctions. The devices are then bonded and integrated in a ceramic chip for further electrical characterizations.

Computational Procedures for Van der Waals Heterostructures. The IPs, EAs, and the Fermi energies and band offsets are calculated *via* combinations of surface, interface, and bulk calculations performed within the framework of KS DFT[74,75] using the projector augmented wave method (PAW) as implemented in the VASP code.[88,89] The exchange−correlation functional is described using the Perdew−Burke−Ernzerhof (PBE) formulation of the generalized-gradient approximation.[90,91] The G_0W_0 method is used to estimate the many-body corrections to the band structure of semiconducting bulk systems.[76,77,91] The "GW" PAW potentials (v54) distributed with the code have been used.[92] Tungsten S semicore states were treated as valence orbitals. A $12 \times 12 \times 3$ Γ-centered *k*-point mesh is used for the Brillouin zone integrations of bulk WS_2 and WSe_2. Equivalently dense meshes are used in all calculations. The electron wave functions are expanded in a plane-wave basis set of 420 eV cutoff energy. G_0W_0 corrections are computed on top of PBE calculations to alleviate the limitation of DFT for the description of semiconductor band gaps. From a practical point of view, it is computationally easier to converge the G_0W_0 correction to the band gap rather than the absolute band positions. As it is known that the many-body corrections to the valence band maximum (VBM) and conduction band minimum (CBM) are rather symmetric, leaving the band gap center largely unaffected, we chose to align the G_0W_0 quasi-particle (QP) band structures with the band-gap center described at the PBE level.[93] An energy cutoff of 280 eV is used for the expansion of the response functions including all unoccupied orbitals. The QP band structures are obtained by interpolation of the $12 \times 12 \times 3$ Γ-centered *k*-point mesh by means of maximally localized Wannier functions.[94] As the orbitals are kept fixed in the G_0W_0 method, the KS potential obtained at the DFT level can be used to realize the electrostatic alignment between the G_0W_0 quasi-particle band structure and the surface and interface DFT calculations.

The IPs of WS_2 and WSe_2 are calculated as the VBM with respect to the vacuum energy level obtained *via* electrostatic alignment with a surface calculation,

$$\epsilon_{IP} = \Delta\epsilon_{vac,ref}|_0 - \Delta\epsilon_{VBM,ref}|_0$$

where ϵ_{IP} is the ionization potential and $\Delta\epsilon_{vac,ref}$ is the energy difference between the Kohn−Sham potential in the vacuum region and a reference energy level taken in the bulk-like region of a surface calculations. $\Delta\epsilon_{VBM,ref}$ is the difference between the VBM and the reference energy level in a bulk calculation. The notation $\Delta\epsilon|_0$ is used to indicate that the energy differences are evaluated in the bulk configuration using experimental lattice constants and internal coordinates. The reference energy level is taken as the average of the KS potential within PAW spheres of W, Co, or Ni sites far from the surface, in bulklike regions. EAs, computed as the CBM with respect to the vacuum energy, are obtained by subtracting the G_0W_0-calculated band gap to IPs. For metallic systems, the ionization potential is identical to the work function (Ni: 5.03 eV, Co: 4.94 eV), and it represents the absolute position of the Fermi energy with respect to the vacuum energy level.

The calculation of the band offsets follows the procedure described by Hinuma *et al.*[84] An interface calculation is performed to give the difference between the reference energy levels of the two constituent materials A and B, $\Delta\epsilon^{A\text{-}B}_{ref}|_x = \Delta\epsilon^{A}_{ref}|_x - \Delta\epsilon^{B}_{ref}|_x$. Here the notation $\Delta\epsilon|_x$ is used to indicate that the calculations are done using a common set of in-plane lattice parameters X, associated with a commensurate interface between A and B. The other lattice parameter and the internal coordinates are optimized. This situation corresponds to a coherent interface, *i.e.*, when the cohesive energy overcomes the energy required to strain the constituent materials and form a commensurate interface.[95] This is not expected to be the case in the device investigated here, where the WS_2 and WSe_2 layers are thick enough to assume complete relief of the interfacial strain. In our case, relaxation of the in-plane lattice parameters should be considered. This correction is achieved by computing the natural band offset defined as

$$\Delta\epsilon^{A-B}_{i,j} = (\Delta\epsilon^{A}_{i,ref}|_0 - \Delta\epsilon^{A}_{vac,ref}|_0 + \Delta\epsilon^{A}_{vac,ref}|_x) + \Delta\epsilon^{A-B}_{ref}|_x - (\Delta\epsilon^{B}_{j,ref}|_0 - \Delta\epsilon^{B}_{vac,ref}|_0 + \Delta\epsilon^{B}_{vac,ref}|_x)$$

Here, *i* and *j* denote the index of the energy levels of interest. One notes that the approach used to estimate the natural band offsets does not account for the increased dielectric screening induced by the metallic electrodes. However, extrapolating from previous theoretical considerations,[96−99] the dielectric modulation of the band gap at the center of our WS_2 and WSe_2 layers is well below 100 meV and, hence, does not affect the overall VBM profile computed across the junction. In practice, the estimation of the natural band offset requires a total of seven calculations including four surfaces and one interface. The surface and interface supercells are built from slabs of five layers of semiconducting WS_2 and WSe_2 and height atomic layers of *fcc*-Ni and *hcp*-Co respectively in the ⟨111⟩ and ⟨0001⟩ directions. The computed commensurate interfaces are depicted in Figure 7. When required for surface and interface calculations a vacuum slab of more than 20 Å is added so as to describe correctly the vacuum energy level and prevent spurious interactions between periodically repeated slabs. The van der Waals interactions are considered in the calculation of atomic forces and stress tensors by adding a correction term to the conventional KS-DFT energy by means of the zero damping DFT-D3 method of Grimme *et al.*[100] The interfaces have been fully relaxed up to atomic forces lower than 0.002 eV/Å.

https://doi.org/10.1021/acsnano.1c00544
ACS Nano XXXX, XXX, XXX−XXX

AUTHOR INFORMATION

Corresponding Authors

Bruno Dlubak − *Unité Mixte de Physique, CNRS, Thales, Université Paris-Saclay, 91767 Palaiseau, France;* orcid.org/0000-0001-5696-8991; Email: bruno.dlubak@cnrs-thales.fr

Pierre Seneor − *Unité Mixte de Physique, CNRS, Thales, Université Paris-Saclay, 91767 Palaiseau, France;* Email: pierre.seneor@cnrs-thales.fr

Authors

Victor Zatko − *Unité Mixte de Physique, CNRS, Thales, Université Paris-Saclay, 91767 Palaiseau, France;* orcid.org/0000-0002-2475-8866

Simon Mutien-Marie Dubois − *Unité Mixte de Physique, CNRS, Thales, Université Paris-Saclay, 91767 Palaiseau, France; Institute of Condensed Matter and Nanosciences (IMCN), Université Catholique de Louvain, B-1348 Louvain-la-Neuve, Belgium*

Florian Godel − *Unité Mixte de Physique, CNRS, Thales, Université Paris-Saclay, 91767 Palaiseau, France;* orcid.org/0000-0003-1741-2741

Cécile Carrétéro − *Unité Mixte de Physique, CNRS, Thales, Université Paris-Saclay, 91767 Palaiseau, France*

Anke Sander − *Unité Mixte de Physique, CNRS, Thales, Université Paris-Saclay, 91767 Palaiseau, France*

Sophie Collin − *Unité Mixte de Physique, CNRS, Thales, Université Paris-Saclay, 91767 Palaiseau, France*

Marta Galbiati − *Unité Mixte de Physique, CNRS, Thales, Université Paris-Saclay, 91767 Palaiseau, France*

Julian Peiro − *Unité Mixte de Physique, CNRS, Thales, Université Paris-Saclay, 91767 Palaiseau, France*

Federico Panciera − *Université Paris-Saclay, CNRS, Centre de Nanosciences et de Nanotechnologies, 91120 Palaiseau, France;* orcid.org/0000-0003-2455-6516

Gilles Patriarche − *Université Paris-Saclay, CNRS, Centre de Nanosciences et de Nanotechnologies, 91120 Palaiseau, France*

Pierre Brus − *Unité Mixte de Physique, CNRS, Thales, Université Paris-Saclay, 91767 Palaiseau, France; Thales Research and Technology, 91767 Palaiseau, France*

Bernard Servet − *Thales Research and Technology, 91767 Palaiseau, France*

Jean-Christophe Charlier − *Institute of Condensed Matter and Nanosciences (IMCN), Université Catholique de Louvain, B-1348 Louvain-la-Neuve, Belgium*

Marie-Blandine Martin − *Unité Mixte de Physique, CNRS, Thales, Université Paris-Saclay, 91767 Palaiseau, France*

Complete contact information is available at: https://pubs.acs.org/10.1021/acsnano.1c00544

Author Contributions

#S.M.-M.D.: first author for theoretical part.

Notes

The authors declare no competing financial interest.

ACKNOWLEDGMENTS

This project has received funding from the European Union's H2020 Future and Emerging Technologies Graphene Flagship (Grant Core3 No. 881603). This research is supported by a public grant overseen by the French National Research Agency (ANR) as part of the "Investissements d'Avenir" program Labex NanoSaclay (ANR-10-LABX-0035) and Equipex TEMPOS (ANR-10-EQPX-0050), as well as by the F.R.S.-FNRS, the "3D nanoarchitecturing of 2D crystals" project (ARC 16/21-077), and by the Flag-ERA JTC 2019 project entitled "SOGraphMEM" (ANR-19-GRFI-0001-07, R.8012.19). Computational resources were provided by the supercomputing facilities of the Université Catholique de Louvain (CISM) and the Consortium des Équipements de Calcul Intensif en Fédération Wallonie Bruxelles (CÉCI) funded by the Fonds de la Recherche Scientifique de Belgique (F.R.S.-FNRS) under the convention No. 2.5020.11.

REFERENCES

(1) Mak, K. F.; Lee, C.; Hone, J.; Shan, J.; Heinz, T. F. Atomically Thin MoS_2: A New Direct-Gap Semiconductor. *Phys. Rev. Lett.* **2010**, *105* (13), 136805.

(2) Splendiani, A.; Sun, L.; Zhang, Y.; Li, T.; Kim, J.; Chim, C. Y.; Galli, G.; Wang, F. Emerging Photoluminescence in Monolayer MoS_2. *Nano Lett.* **2010**, *10* (4), 1271−1275.

(3) Radisavljevic, B.; Radenovic, A.; Brivio, J.; Giacometti, V.; Kis, A. Single-Layer MoS_2 Transistors. *Nat. Nanotechnol.* **2011**, *6* (3), 147−150.

(4) Piquemal-Banci, M.; Galceran, R.; Martin, M.-B.; Godel, F.; Anane, A.; Petroff, F.; Dlubak, B.; Seneor, P. 2D-MTJs: Introducing 2D Materials in Magnetic Tunnel Junctions. *J. Phys. D: Appl. Phys.* **2017**, *50* (20), 203002.

(5) Castellanos-Gomez, A. Why All the Fuss about 2D Semiconductors? *Nat. Photonics* **2016**, *10* (4), 202−204.

(6) Geim, A. K.; Grigorieva, I. V. van der Waals Heterostructures. *Nature* **2013**, *499* (7459), 419−425.

(7) Novoselov, K. S.; Mishchenko, A.; Carvalho, A.; Castro Neto, A. H. 2D Materials and van der Waals Heterostructures. *Science* **2016**, *353* (6298), No. aac9439.

(8) Chaves, A.; Azadani, J. G.; Alsalman, H.; da Costa, D. R.; Frisenda, R.; Chaves, A. J.; Song, S. H.; Kim, Y. D.; He, D.; Zhou, J.; Castellanos-Gomez, A.; Peeters, F. M.; Liu, Z.; Hinkle, C. L.; Oh, S. H.; Ye, P. D.; Koester, S. J.; Lee, Y. H.; Avouris, P.; Wang, X.; Low, T. Bandgap Engineering of Two-Dimensional Semiconductor Materials. *npj 2D Mater. Appl.* **2020**, *4* (1), 1−21.

(9) Capasso, F. Band-Gap Engineering: From Physics and Materials to New Semiconductor Devices. *Science* **1987**, *235* (4785), 172−176.

(10) Levine, B. F. Quantum-Well Infrared Photodetectors. *J. Appl. Phys.* **1993**, *74* (8), R1−R81.

(11) Faist, J.; Capasso, F.; Sivco, D. L.; Sirtori, C.; Hutchinson, A. L.; Cho, A. Y. Quantum Cascade Laser. *Science* **1994**, *264* (5158), 553−556.

(12) Gendron, L.; Carras, M.; Huynh, A.; Ortiz, V.; Koeniguer, C.; Berger, V. Quantum Cascade Photodetector. *Appl. Phys. Lett.* **2004**, *85* (14), 2824−2826.

(13) De Santis, L.; Antón, C.; Reznychenko, B.; Somaschi, N.; Coppola, G.; Senellart, J.; Gómez, C.; Lemaître, A.; Sagnes, I.; White, A. G.; Lanco, L.; Auffèves, A.; Senellart, P. A Solid-State Single-Photon Filter. *Nat. Nanotechnol.* **2017**, *12* (7), 663−667.

(14) Nedelcu, A.; Bonvalot, C.; Taalat, R.; Fantini, J.; Colin, T.; Muller, P.; Huet, O.; Dua, L.; Laurent, T.; Blin, C.; Le Priol, A.; Coussement, J.; Bettiati, M.; Garabédian, P. III-V Detector Technologies at Sofradir: Dealing with Image Quality. *Infrared Phys. Technol.* **2018**, *94*, 273−279.

(15) Khalatpour, A.; Paulsen, A. K.; Deimert, C.; Wasilewski, Z. R.; Hu, Q. High-Power Portable Terahertz Laser Systems. *Nat. Photonics* **2021**, *15*, 16−20.

(16) Ataca, C.; Şahin, H.; Ciraci, S. Stable, Single-Layer MX_2 Transition-Metal Oxides and Dichalcogenides in a Honeycomb-Like Structure. *J. Phys. Chem. C* **2012**, *116* (16), 8983−8999.

(17) Mounet, N.; Gibertini, M.; Schwaller, P.; Campi, D.; Merkys, A.; Marrazzo, A.; Sohier, T.; Castelli, I. E.; Cepellotti, A.; Pizzi, G.; Marzari, N. Two-Dimensional Materials from High-Throughput

Computational Exfoliation of Experimentally Known Compounds. *Nat. Nanotechnol.* **2018**, *13* (3), 246−252.
(18) Zhou, X.; Hang, Y.; Liu, L.; Zhang, Z.; Guo, W. A Large Family of Synthetic Two-Dimensional Metal Hydrides. *J. Am. Chem. Soc.* **2019**, *141* (19), 7899−7905.
(19) Carr, S.; Massatt, D.; Fang, S.; Cazeaux, P.; Luskin, M.; Kaxiras, E. Twistronics: Manipulating the Electronic Properties of Two-Dimensional Layered Structures through Their Twist Angle. *Phys. Rev. B: Condens. Matter Mater. Phys.* **2017**, *95* (7), 075420.
(20) Geng, W. T.; Wang, V.; Lin, J. B.; Ohno, T.; Nara, J. Angle-Dependence of Interlayer Coupling in Twisted Transition Metal Dichalcogenide Heterobilayers. *J. Phys. Chem. C* **2021**, *125* (1), 1048−1053.
(21) Avsar, A.; Tan, J. Y.; Taychatanapat, T.; Balakrishnan, J.; Koon, G. K. W.; Yeo, Y.; Lahiri, J.; Carvalho, A.; Rodin, A. S.; O'Farrell, E. C. T.; Eda, G.; Castro Neto, A. H.; Özyilmaz, B. Spin-Orbit Proximity Effect in Graphene. *Nat. Commun.* **2014**, *5*, 4875.
(22) Wilson, N. R.; Nguyen, P. V.; Seyler, K.; Rivera, P.; Marsden, A. J.; Laker, Z. P. L.; Constantinescu, G. C.; Kandyba, V.; Barinov, A.; Hine, N. D. M.; Xu, X.; Cobden, D. H. Determination of Band Offsets, Hybridization, and Exciton Binding in 2D Semiconductor Heterostructures. *Sci. Adv.* **2017**, *3* (2), No. e1601832.
(23) Piquemal-Banci, M.; Galceran, R.; Godel, F.; Caneva, S.; Martin, M.-B.; Weatherup, R. S.; Kidambi, P. R.; Bouzehouane, K.; Xavier, S.; Anane, A.; Petroff, F.; Fert, A.; Dubois, S. M.-M.; Charlier, J.-C.; Robertson, J.; Hofmann, S.; Dlubak, B.; Seneor, P. Insulator-to-Metallic Spin-Filtering in 2D-Magnetic Tunnel Junctions Based on Hexagonal Boron Nitride. *ACS Nano* **2018**, *12* (5), 4712−4718.
(24) Hunt, B.; Sanchez-Yamagishi, J. D.; Young, A. F.; Yankowitz, M.; LeRoy, B. J.; Watanabe, K.; Taniguchi, T.; Moon, P.; Koshino, M.; Jarillo-Herrero, P.; Ashoori, R. C. Massive Dirac Fermions and Hofstadter Butterfly in a van der Waals Heterostructure. *Science* **2013**, *340* (6139), 1427−1430.
(25) Cao, Y.; Fatemi, V.; Fang, S.; Watanabe, K.; Taniguchi, T.; Kaxiras, E.; Jarillo-Herrero, P. Unconventional Superconductivity in Magic-Angle Graphene Superlattices. *Nature* **2018**, *556* (7699), 43−50.
(26) Rickhaus, P.; Wallbank, J.; Slizovskiy, S.; Pisoni, R.; Overweg, H.; Lee, Y.; Eich, M.; Liu, M. H.; Watanabe, K.; Taniguchi, T.; Ihn, T.; Ensslin, K. Transport through a Network of Topological Channels in Twisted Bilayer Graphene. *Nano Lett.* **2018**, *18* (11), 6725−6730.
(27) Wong, D.; Nuckolls, K. P.; Oh, M.; Lian, B.; Xie, Y.; Jeon, S.; Watanabe, K.; Taniguchi, T.; Bernevig, B. A.; Yazdani, A. Cascade of Electronic Transitions in Magic-Angle Twisted Bilayer Graphene. *Nature* **2020**, *582* (7811), 198−202.
(28) de Vries, F. K.; Portoles, E.; Zheng, G.; Taniguchi, T.; Watanabe, K.; Ihn, T.; Ensslin, K.; Rickhaus, P. Gate-Defined Josephson Junctions in Magic-Angle Twisted Bilayer Graphene. 2020 2011.00011. *Arxiv*. https://arxiv.org/abs/2011.00011 (accessed March 5, 2021).
(29) Zheng, Z.; Ma, Q.; Bi, Z.; de la Barrera, S.; Liu, M. H.; Mao, N.; Zhang, Y.; Kiper, N.; Watanabe, K.; Taniguchi, T.; Kong, J.; Tisdale, W. A.; Ashoori, R.; Gedik, N.; Fu, L.; Xu, S. Y.; Jarillo-Herrero, P. Unconventional Ferroelectricity in Moiré Heterostructures. *Nature* **2020**, *588* (7836), 71−76.
(30) Guo, J.; Wang, L.; Yu, Y.; Wang, P.; Huang, Y.; Duan, X. SnSe/MoS_2 van der Waals Heterostructure Junction Field-Effect Transistors with Nearly Ideal Subthreshold Slope. *Adv. Mater.* **2019**, *31* (49), 1902962.
(31) Almadori, Y.; Bendiab, N.; Grévin, B. Multimodal Kelvin Probe Force Microscopy Investigations of a Photovoltaic WSe_2/MoS_2 Type-II Interface. *ACS Appl. Mater. Interfaces* **2018**, *10* (1), 1363−1373.
(32) Unuchek, D.; Ciarrocchi, A.; Avsar, A.; Watanabe, K.; Taniguchi, T.; Kis, A. Room-Temperature Electrical Control of Exciton Flux in a van der Waals Heterostructure. *Nature* **2018**, *560* (7718), 340−344.
(33) Chappert, C.; Fert, A.; Van Dau, F. N. The Emergence of Spin Electronics in Data Storage. *Nat. Mater.* **2007**, *6* (11), 813−823.
(34) Khvalkovskiy, A. V.; Apalkov, D.; Watts, S.; Chepulskii, R.; Beach, R. S.; Ong, A.; Tang, X.; Driskill-Smith, A.; Butler, W. H.; Visscher, P. B.; Lottis, D.; Chen, E.; Nikitin, V.; Krounbi, M. Basic Principles of STT-MRAM Cell Operation in Memory Arrays. *J. Phys. D: Appl. Phys.* **2013**, *46* (7), 074001.
(35) Dieny, B.; Prejbeanu, I. L.; Garello, K.; Gambardella, P.; Freitas, P.; Lehndorff, R.; Raberg, W.; Ebels, U.; Demokritov, S. O.; Akerman, J.; Deac, A.; Pirro, P.; Adelmann, C.; Anane, A.; Chumak, A. V.; Hiroata, A.; Mangin, S.; Onbasli, M. C.; Aquino, M. d; Prenat, G.; et al. Opportunities and Challenges for Spintronics in the Microelectronic Industry. *Nat. Electron.* **2020**, *3*, 446−459.
(36) Behin-Aein, B.; Datta, D.; Salahuddin, S.; Datta, S. Proposal for an All-Spin Logic Device with Built-In Memory. *Nat. Nanotechnol.* **2010**, *5* (4), 266−270.
(37) Manipatruni, S.; Nikonov, D. E.; Lin, C. C.; Gosavi, T. A.; Liu, H.; Prasad, B.; Huang, Y. L.; Bonturim, E.; Ramesh, R.; Young, I. A. Scalable Energy-Efficient Magnetoelectric Spin−Orbit Logic. *Nature* **2019**, *565* (7737), 35−42.
(38) Borders, W. A.; Pervaiz, A. Z.; Fukami, S.; Camsari, K. Y.; Ohno, H.; Datta, S. Integer Factorization Using Stochastic Magnetic Tunnel Junctions. *Nature* **2019**, *573* (7774), 390−393.
(39) Torrejon, J.; Riou, M.; Araujo, F. A.; Tsunegi, S.; Khalsa, G.; Querlioz, D.; Bortolotti, P.; Cros, V.; Yakushiji, K.; Fukushima, A.; Kubota, H.; Yuasa, S.; Stiles, M. D.; Grollier, J. Neuromorphic Computing with Nanoscale Spintronic Oscillators. *Nature* **2017**, *547* (7664), 428−431.
(40) Awschalom, D. D.; Bassett, L. C.; Dzurak, A. S.; Hu, E. L.; Petta, J. R. Quantum Spintronics: Engineering and Manipulating Atom-Like Spins in Semiconductors. *Science* **2013**, *339* (6124), 1174−1179.
(41) Roche, S.; Åkerman, J.; Beschoten, B.; Charlier, J.-C.; Chshiev, M.; Dash, S. P.; Dlubak, B.; Fabian, J.; Fert, A.; Guimarães, M.; Guinea, F.; Grigorieva, I.; Schönenberger, C.; Seneor, P.; Stampfer, C.; Valenzuela, S. O.; Waintal, X.; Van Wees, B. Graphene Spintronics: The European Flagship Perspective. *2D Mater.* **2015**, *2* (3), 030202.
(42) Zatko, V.; Galbiati, M.; Dubois, S. M.-M.; Och, M.; Palczynski, P.; Mattevi, C.; Brus, P.; Bezencenet, O.; Martin, M.-B.; Servet, B.; Charlier, J.-C.; Godel, F.; Vecchiola, A.; Bouzehouane, K.; Collin, S.; Petroff, F.; Dlubak, B.; Seneor, P. Band-Structure Spin-Filtering in Vertical Spin Valves Based on Chemical Vapor Deposited WS_2. *ACS Nano* **2019**, *13* (12), 14468−14476.
(43) Yang, H.; Vu, A. D.; Hallal, A.; Rougemaille, N.; Coraux, J.; Chen, G.; Schmid, A. K.; Chshiev, M. Anatomy and Giant Enhancement of the Perpendicular Magnetic Anisotropy of Cobalt−Graphene Heterostructures. *Nano Lett.* **2016**, *16* (1), 145−151.
(44) Vu, A. D.; Coraux, J.; Chen, G.; N'Diaye, A. T.; Schmid, A. K.; Rougemaille, N. Unconventional Magnetisation Texture in Graphene/Cobalt Hybrids. *Sci. Rep.* **2016**, *6* (1), 24783.
(45) Naganuma, H.; Zatko, V.; Galbiati, M.; Godel, F.; Sander, A.; Carrétéro, C.; Bezencenet, O.; Reyren, N.; Martin, M.-B.; Dlubak, B.; Seneor, P. A Perpendicular Graphene/Ferromagnet Electrode for Spintronics. *Appl. Phys. Lett.* **2020**, *116* (17), 173101.
(46) Lv, W.; Jia, Z.; Wang, B.; Lu, Y.; Luo, X.; Zhang, B.; Zeng, Z.; Liu, Z. Electric-Field Control of Spin-Orbit Torques in WS_2/Permalloy Bilayers. *ACS Appl. Mater. Interfaces* **2018**, *10* (3), 2843−2849.
(47) Yang, H.; Chen, G.; Cotta, A. A. C.; N'DIaye, A. T.; Nikolaev, S. A.; Soares, E. A.; MacEdo, W. A. A.; Liu, K.; Schmid, A. K.; Fert, A.; Chshiev, M. Significant Dzyaloshinskii-Moriya Interaction at Graphene-Ferromagnet Interfaces Due to the Rashba Effect. *Nat. Mater.* **2018**, *17* (7), 605−609.
(48) Liang, J.; Wang, W.; Du, H.; Hallal, A.; Garcia, K.; Chshiev, M.; Fert, A.; Yang, H. Very Large Dzyaloshinskii-Moriya Interaction in Two-Dimensional Janus Manganese Dichalcogenides and Its Application to Realize Skyrmion States. *Phys. Rev. B: Condens. Matter Mater. Phys.* **2020**, *101* (18), 184401.
(49) Novoselov, K. S.; Geim, A. K.; Morozov, S. V.; Jiang, D.; Zhang, Y.; Dubonos, S. V.; Grigorieva, I. V.; Firsov, A. A. Electric

https://doi.org/10.1021/acsnano.1c00544
ACS Nano XXXX, XXX, XXX−XXX

Field in Atomically Thin Carbon Films. *Science* **2004**, *306* (5696), 666−669.
(50) Guo, H.; Hu, Z.; Liu, Z.; Tian, J. Stacking of 2D Materials. *Adv. Funct. Mater.* **2021**, *31* (4), 2007810.
(51) Galbiati, M.; Tatay, S.; Dubois, S. M.-M.; Godel, F.; Galceran, R.; Mañas-Valero, S.; Piquemal-Banci, M.; Vecchiola, A.; Charlier, J.-C.; Forment-Aliaga, A.; Coronado, E.; Dlubak, B.; Seneor, P. Path to Overcome Material and Fundamental Obstacles in Spin Valves Based on MoS_2 and Other Transition-Metal Dichalcogenides. *Phys. Rev. Appl.* **2019**, *12* (4), 044022.
(52) Mattevi, C.; Kim, H.; Chhowalla, M. A Review of Chemical Vapour Deposition of Graphene on Copper. *J. Mater. Chem.* **2011**, *21* (10), 3324−3334.
(53) Kidambi, P. R.; Ducati, C.; Dlubak, B.; Gardiner, D.; Weatherup, R. S.; Martin, M. B.; Seneor, P.; Coles, H.; Hofmann, S. The Parameter Space of Graphene Chemical Vapor Deposition on Polycrystalline Cu. *J. Phys. Chem. C* **2012**, *116* (42), 22492−22501.
(54) Weatherup, R. S.; Dlubak, B.; Hofmann, S. Kinetic Control of Catalytic CVD for High-Quality Graphene at Low Temperatures. *ACS Nano* **2012**, *6* (11), 9996−10003.
(55) Caneva, S.; Weatherup, R. S.; Bayer, B. C.; Blume, R.; Cabrero-Vilatela, A.; Braeuninger-Weimer, P.; Martin, M.-B.; Wang, R.; Baehtz, C.; Schloegl, R.; Meyer, J. C.; Hofmann, S. Controlling Catalyst Bulk Reservoir Effects for Monolayer Hexagonal Boron Nitride CVD. *Nano Lett.* **2016**, *16* (2), 1250−1261.
(56) Reale, F.; Palczynski, P.; Amit, I.; Jones, G. F.; Mehew, J. D.; Bacon, A.; Ni, N.; Sherrell, P. C.; Agnoli, S.; Craciun, M. F.; Russo, S.; Mattevi, C. High-Mobility and High-Optical Quality Atomically Thin WS_2. *Sci. Rep.* **2017**, *7* (1), 14911.
(57) Zhou, J.; Lin, J.; Huang, X.; Zhou, Y.; Chen, Y.; Xia, J.; Wang, H.; Xie, Y.; Yu, H.; Lei, J.; Wu, D.; Liu, F.; Fu, Q.; Zeng, Q.; Hsu, C. H.; Yang, C.; Lu, L.; Yu, T.; Shen, Z.; Lin, H.; et al. A Library of Atomically Thin Metal Chalcogenides. *Nature* **2018**, *556* (7701), 355−359.
(58) Serna, M. I.; Yoo, S. H.; Moreno, S.; Xi, Y.; Oviedo, J. P.; Choi, H.; Alshareef, H. N.; Kim, M. J.; Minary-Jolandan, M.; Quevedo-Lopez, M. A. Large-Area Deposition of MoS_2 by Pulsed Laser Deposition with *in Situ* Thickness Control. *ACS Nano* **2016**, *10* (6), 6054−6061.
(59) Loh, T. A. J.; Chua, D. H. C.; Wee, A. T. S. One-Step Synthesis of Few-Layer WS_2 by Pulsed Laser Deposition. *Sci. Rep.* **2016**, *5* (1), 18116.
(60) Nakano, M.; Wang, Y.; Kashiwabara, Y.; Matsuoka, H.; Iwasa, Y. Layer-by-Layer Epitaxial Growth of Scalable WSe_2 on Sapphire by Molecular Beam Epitaxy. *Nano Lett.* **2017**, *17* (9), 5595−5599.
(61) Yan, M.; Wang, E.; Zhou, X.; Zhang, G.; Zhang, H.; Zhang, K.; Yao, W.; Lu, N.; Yang, S.; Wu, S.; Yoshikawa, T.; Miyamoto, K.; Okuda, T.; Wu, Y.; Yu, P.; Duan, W.; Zhou, S. High Quality Atomically Thin $PtSe_2$ Films Grown by Molecular Beam Epitaxy. *2D Mater.* **2017**, *4* (4), 045015.
(62) Godel, F.; Zatko, V.; Carrétéro, C.; Sander, A.; Galbiati, M.; Vecchiola, A.; Brus, P.; Bezencenet, O.; Servet, B.; Martin, M.-B.; Dlubak, B.; Seneor, P. WS_2 2D Semiconductor down to Monolayers by Pulsed-Laser Deposition for Large-Scale Integration in Electronics and Spintronics Circuits. *ACS Appl. Nano Mater.* **2020**, *3* (8), 7908−7916.
(63) Govind Rajan, A.; Warner, J. H.; Blankschtein, D.; Strano, M. S. Generalized Mechanistic Model for the Chemical Vapor Deposition of 2D Transition Metal Dichalcogenide Monolayers. *ACS Nano* **2016**, *10* (4), 4330−4344.
(64) Lee, J.; Pak, S.; Giraud, P.; Lee, Y.-W.; Cho, Y.; Hong, J.; Jang, A.-R.; Chung, H.-S.; Hong, W.-K.; Jeong, H. Y.; Shin, H. S.; Occhipinti, L. G.; Morris, S. M.; Cha, S.; Sohn, J. I.; Kim, J. M. Thermodynamically Stable Synthesis of Large-Scale and Highly Crystalline Transition Metal Dichalcogenide Monolayers and Their Unipolar *n-n* Heterojunction Devices. *Adv. Mater.* **2017**, *29* (33), 1702206.
(65) Berkdemir, A.; Gutiérrez, H. R.; Botello-Méndez, A. R.; Perea-López, N.; Elías, A. L.; Chia, C. I.; Wang, B.; Crespi, V. H.; López-Urías, F.; Charlier, J. C.; Terrones, H.; Terrones, M. Identification of Individual and Few Layers of WS_2 Using Raman Spectroscopy. *Sci. Rep.* **2013**, *3* (1), 1755.
(66) Sahin, H.; Tongay, S.; Horzum, S.; Fan, W.; Zhou, J.; Li, J.; Wu, J.; Peeters, F. M. Anomalous Raman Spectra and Thickness-Dependent Electronic Properties of WSe_2. *Phys. Rev. B: Condens. Matter Mater. Phys.* **2013**, *87* (16), 165409.
(67) Tonndorf, P.; Schmidt, R.; Böttger, P.; Zhang, X.; Börner, J.; Liebig, A.; Albrecht, M.; Kloc, C.; Gordan, O.; Zahn, D. R. T.; Michaelis de Vasconcellos, S.; Bratschitsch, R. Photoluminescence Emission and Raman Response of Monolayer MoS_2, $MoSe_2$, and WSe_2. *Opt. Express* **2013**, *21* (4), 4908.
(68) Del Corro, E.; Terrones, H.; Elias, A.; Fantini, C.; Feng, S.; Nguyen, M. A.; Mallouk, T. E.; Terrones, M.; Pimenta, M. A. Excited Excitonic States in 1L, 2L, 3L, and Bulk WSe_2 Observed by Resonant Raman Spectroscopy. *ACS Nano* **2014**, *8* (9), 9629−9635.
(69) Haigh, S. J.; Gholinia, A.; Jalil, R.; Romani, S.; Britnell, L.; Elias, D. C.; Novoselov, K. S.; Ponomarenko, L. A.; Geim, A. K.; Gorbachev, R. Cross-Sectional Imaging of Individual Layers and Buried Interfaces of Graphene-Based Heterostructures and Superlattices. *Nat. Mater.* **2012**, *11* (9), 764−767.
(70) Bunch, J. S.; Verbridge, S. S.; Alden, J. S.; van der Zande, A. M.; Parpia, J. M.; Craighead, H. G.; McEuen, P. L. Impermeable Atomic Membranes from Graphene Sheets. *Nano Lett.* **2008**, *8* (8), 2458−2462.
(71) Dlubak, B.; Martin, M.-B.; Weatherup, R. S.; Yang, H.; Deranlot, C.; Blume, R.; Schloegl, R.; Fert, A.; Anane, A.; Hofmann, S.; Seneor, P.; Robertson, J. Graphene-Passivated Nickel as an Oxidation-Resistant Electrode for Spintronics. *ACS Nano* **2012**, *6* (12), 10930−10934.
(72) Piquemal-Banci, M.; Galceran, R.; Dubois, S. M.-M.; Zatko, V.; Galbiati, M.; Godel, F.; Martin, M.-B.; Weatherup, R. S.; Petroff, F.; Fert, A.; Charlier, J.-C.; Robertson, J.; Hofmann, S.; Dlubak, B.; Seneor, P. Spin Filtering by Proximity Effects at Hybridized Interfaces in Spin-Valves with 2D Graphene Barriers. *Nat. Commun.* **2020**, *11* (1), 5670.
(73) Yun, W. S.; Han, S. W.; Hong, S. C.; Kim, I. G.; Lee, J. D. Thickness and Strain Effects on Electronic Structures of Transition Metal Dichalcogenides: 2H-MX_2 Semiconductors (M = Mo, W; X = S, Se, Te). *Phys. Rev. B: Condens. Matter Mater. Phys.* **2012**, *85* (3), 033305.
(74) Hohenberg, P.; Kohn, W. Inhomogeneous Electron Gas. *Phys. Rev.* **1964**, *136* (3B), B864.
(75) Kohn, W.; Sham, L. J. Self-Consistent Equations Including Exchange and Correlation Effects. *Phys. Rev.* **1965**, *140* (4A), A1133.
(76) Hedin, L. New Method for Calculating the One-Particle Green's Function with Application to the Electron-Gas Problem. *Phys. Rev.* **1965**, *139* (3A), A796.
(77) Hybertsen, M. S.; Louie, S. G. Electron Correlation in Semiconductors and Insulators: Band Gaps and Quasiparticle Energies. *Phys. Rev. B: Condens. Matter Mater. Phys.* **1986**, *34* (8), 5390−5413.
(78) Schutte, W. J.; De Boer, J. L.; Jellinek, F. Crystal Structures of Tungsten Disulfide and Diselenide. *J. Solid State Chem.* **1987**, *70* (2), 207−209.
(79) Jiang, H. Electronic Band Structures of Molybdenum and Tungsten Dichalcogenides by the GW Approach. *J. Phys. Chem. C* **2012**, *116* (14), 7664−7671.
(80) Ballif, C.; Regula, M.; Schmid, P. E.; Remškar, M.; Sanjinés, R.; Lévy, F. Preparation and Characterization of Highly Oriented, Photoconducting WS2 Thin Films. *Appl. Phys. A: Mater. Sci. Process.* **1996**, *62* (6), 543−546.
(81) Li, S. J.; Bernède, J. C.; Pouzet, J.; Jamali, M. WS_2 Thin Films Prepared by Solid State Reaction (Induced by Annealing) between the Constituents in Thin Film Form. *J. Phys.: Condens. Matter* **1996**, *8* (14), 2291−2304.
(82) Finteis, T.; Hengsberger, M.; Straub, T.; Fauth, K.; Claessen, R.; Auer, P.; Steiner, P.; Hüfner, S.; Blaha, P.; Vögt, M.; Lux-Steiner, M.; Bucher, E. Occupied and Unoccupied Electronic Band Structure

https://doi.org/10.1021/acsnano.1c00544
ACS Nano XXXX, XXX, XXX−XXX

of WSe_2. *Phys. Rev. B: Condens. Matter Mater. Phys.* **1997**, *55* (16), 10400−10411.
(83) Schlaf, R.; Lang, O.; Pettenkofer, C.; Jaegermann, W. Band Lineup of Layered Semiconductor Heterointerfaces Prepared by van der Waals Epitaxy: Charge Transfer Correction Term for the Electron Affinity Rule. *J. Appl. Phys.* **1999**, *85* (5), 2732−2753.
(84) Hinuma, Y.; Grüneis, A.; Kresse, G.; Oba, F. Band Alignment of Semiconductors from Density-Functional Theory and Many-Body Perturbation Theory. *Phys. Rev. B: Condens. Matter Mater. Phys.* **2014**, *90* (15), 155405.
(85) Tsen, A. W.; Brown, L.; Havener, R. W.; Park, J. Polycrystallinity and Stacking in CVD Graphene. *Acc. Chem. Res.* **2013**, *46* (10), 2286−2296.
(86) Lu, C. C.; Lin, Y. C.; Liu, Z.; Yeh, C. H.; Suenaga, K.; Chiu, P. W. Twisting Bilayer Graphene Superlattices. *ACS Nano* **2013**, *7* (3), 2587−2594.
(87) Pezzini, S.; Mišeikis, V.; Piccinini, G.; Forti, S.; Pace, S.; Engelke, R.; Rossella, F.; Watanabe, K.; Taniguchi, T.; Kim, P.; Coletti, C. 30°-Twisted Bilayer Graphene Quasicrystals from Chemical Vapor Deposition. *Nano Lett.* **2020**, *20* (5), 3313−3319.
(88) Kresse, G.; Furthmüller, J. Efficient Iterative Schemes for *ab Initio* Total-Energy Calculations Using a Plane-Wave Basis Set. *Phys. Rev. B: Condens. Matter Mater. Phys.* **1996**, *54* (16), 11169−11186.
(89) Kresse, G.; Joubert, D. From Ultrasoft Pseudopotentials to the Projector Augmented-Wave Method. *Phys. Rev. B: Condens. Matter Mater. Phys.* **1999**, *59* (3), 1758−1775.
(90) Perdew, J. P.; Burke, K.; Ernzerhof, M. Generalized Gradient Approximation Made Simple. *Phys. Rev. Lett.* **1996**, *77* (18), 3865−3868.
(91) Klimeš, J.; Kaltak, M.; Kresse, G. Predictive GW Calculations Using Plane Waves and Pseudopotentials. *Phys. Rev. B: Condens. Matter Mater. Phys.* **2014**, *90* (7), 075125.
(92) Shishkin, M.; Kresse, G. Implementation and Performance of the Frequency-Dependent GW Method within the PAW Framework. *Phys. Rev. B: Condens. Matter Mater. Phys.* **2006**, *74* (3), 035101.
(93) Toroker, M. C.; Kanan, D. K.; Alidoust, N.; Isseroff, L. Y.; Liao, P.; Carter, E. A. First Principles Scheme to Evaluate Band Edge Positions in Potential Transition Metal Oxide Photocatalysts and Photoelectrodes. *Phys. Chem. Chem. Phys.* **2011**, *13* (37), 16644−16654.
(94) Mostofi, A. A.; Yates, J. R.; Pizzi, G.; Lee, Y. S.; Souza, I.; Vanderbilt, D.; Marzari, N. An Updated Version of Wannier90: A Tool for Obtaining Maximally-Localised Wannier Functions. *Comput. Phys. Commun.* **2014**, *185* (8), 2309−2310.
(95) Van Troeye, B.; Lherbier, A.; Dubois, S. M.-M.; Charlier, J.-C.; Gonze, X. First-Principles Prediction of Lattice Coherency in van der Waals Heterostructures. 2019, 1911.06846. *Arxiv*. https://arxiv.org/abs/1911.06846 (accessed March 5, 2021).
(96) Cho, Y.; Berkelbach, T. C. Environmentally Sensitive Theory of Electronic and Optical Transitions in Atomically Thin Semiconductors. *Phys. Rev. B: Condens. Matter Mater. Phys.* **2018**, *97* (4), 041409.
(97) Gerber, I. C.; Marie, X. Dependence of the HBN Layer Thickness on the Band Structure and Exciton Properties of Encapsulated WSe_2 Monolayers. *Phys. Rev. B: Condens. Matter Mater. Phys.* **2018**, *98*, 245126.
(98) Meckbach, L.; Stroucken, T.; Koch, S. W. Influence of the Effective Layer Thickness on the Ground-State and Excitonic Properties of Transition-Metal Dichalcogenide Systems. *Phys. Rev. B: Condens. Matter Mater. Phys.* **2018**, *97* (3), 035425.
(99) Winther, K. T.; Thygesen, K. S. Band Structure Engineering in van der Waals Heterostructures *via* Dielectric Screening: The GΔW Method. *2D Mater.* **2017**, *4* (2), 025059.
(100) Grimme, S.; Antony, J.; Ehrlich, S.; Krieg, H. A Consistent and Accurate *ab Initio* Parametrization of Density Functional Dispersion Correction (DFT-D) for the 94 Elements H-Pu. *J. Chem. Phys.* **2010**, *132* (15), 154104.

https://doi.org/10.1021/acsnano.1c00544
ACS Nano XXXX, XXX, XXX−XXX